

Development of a ReaxFF Reactive Force Field for Ettringite and Study of its Mechanical Failure Modes from Reactive Dynamics Simulations

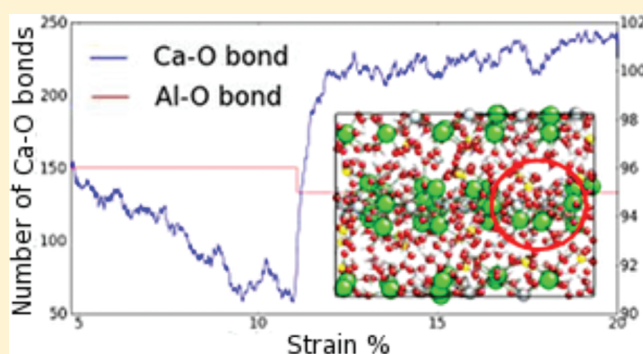
Lianchi Liu,[†] Andres Jaramillo-Botero,^{*‡} William A. Goddard, III,^{*‡} and Huai Sun[†]

[†]Computational Chemistry Group, School of Chemistry and Chemical Engineering, Shanghai Jiao Tong University, 800 Dongchuan Road, Min Hang, Shanghai 200240, China

[‡]Materials and Process Simulation Center (MC 139-74), Chemistry and Chemical Engineering Division, California Institute of Technology, 1200 East California Boulevard, Pasadena, California 91125, United States

S Supporting Information

ABSTRACT: Ettringite is a hexacalcium aluminate trisulfate hydrate mineral that forms during Portland cement hydration. Its presence plays an important role in controlling the setting rate of the highly reactive aluminate phases in cement paste and has also been associated with severe cracking in cured hardened cement. To understand how it forms and how its properties influence those of hardened cement and concrete, we have developed a first-principles-based ReaxFF reactive force field for Ca/Al/H/O/S. Here, we report on the development of this ReaxFF force field and on its validation and application using reactive molecular dynamics (RMD) simulations to characterize and understand the elastic, plastic, and failure response of ettringite at the atomic scale. The ReaxFF force field was validated by comparing the lattice parameters, pairwise distribution functions, and elastic constants of an ettringite crystal model obtained from RMD simulations with those from experiments. The predicted results are in close agreement with published experimental data. To characterize the atomistic failure modes of ettringite, we performed stress–strain simulations to find that Ca–O bonds are responsible for failure of the calcium sulfate and tricalcium aluminate (C3A) column in ettringite during uniaxial compression and tension and that hydrogen bond re-formation during compression induces an increase in plastic strain beyond the material's stress–strain proportionality limit. These results provide essential insight into understanding the mechanistic role of this mineral in cement and concrete degradation, and the ReaxFF potential developed in this work serves as a fundamental tool to further study the kinetics of hydration in cement and concrete.



1. INTRODUCTION

The trisulfate mineral ettringite, with chemical formula $\text{Ca}_6[\text{Al}(\text{OH})_6]_2(\text{SO}_4)_3 \cdot 26\text{H}_2\text{O}$, is a precipitate formed in hydrated Portland cement as a result of the reaction of calcium aluminate (A) with calcium sulfate (C), and its presence depends on the ratio C3A. Changes in this ratio as well as the permeability of ettringite to water and its reactions with other chemical species (e.g., sulfates) affect its structural evolution during cement hydration and, consequently, cement properties. The formation of ettringite during the early cement hydration stage plays an important role in controlling the setting rate of the highly reactive aluminate phases. Its formation results in a volume increase in the fresh, plastic concrete, which has also been associated spatially with severe cracking in cured hardened concrete¹ during what is referred to as delayed ettringite formation, or DEF, and during cement degradation via sulfate attacks.²

To help settle the mechanistic issues, it would be most useful to understand the atomistic processes involved with mechan-

ically loaded ettringite. However, the quantum mechanics (QM) methods usually applied to studies of chemical reaction processes are not capable of treating the spatial and time scales involved. Consequently, we have used QM to train the parameters of a ReaxFF³ reactive force field and then used it to simulate the physical properties and reaction processes that occur during ettringite loading.

This paper focuses on investigating the chemical processes relevant to the mechanical properties of ettringite, including its failure modes under pressure loading, using reactive molecular dynamics (RMD). We first develop the ReaxFF first-principles-based reactive force field to describe the structures, energetics, and forces from QM on prototypical systems. Then, we carried out RMD to study the decomposition and growth of various phases over a broad set of conditions. In section 2.1.1, we

Received: October 21, 2011

Revised: February 27, 2012

64 describe the ReaxFF reactive force field developed (see
65 Supporting Information), and section 3.1 provides a description
66 of several validation tests performed on ettringite. Then, in
67 section 3.2, we describe how ReaxFF was used to characterize
68 the mechanical response and failure modes of ettringite under
69 strain loading. We consider that these modes of failure are
70 critical to understand and control the long-term properties of
71 Portland-based concrete structures.

2. COMPUTATIONAL DETAILS

72 Modern QM methods provide reaction surfaces and geometries
73 of molecular systems sufficiently accurate to predict a reaction
74 mechanism in advance of experiment. However, scaling of
75 computational cost with system size (i.e., the number of atoms)
76 limits these methods to within ~ 100 atoms. QM can be used to
77 derive the forces for describing the dynamical equations of
78 motion of all particles involved; however, again, computational
79 costs restrict the time scale to a few picoseconds. This stems
80 from the high cost of solving self-consistently the Schrödinger
81 equation for all nuclear and electronic interactions. Con-
82 sequently, the use of QM to study the reaction processes
83 occurring in ettringite as the system is dynamically strain
84 loaded/unloaded is well beyond the current practical limits of
85 QM calculations.

86 **2.1. ReaxFF Force Field.** To provide a practical solution to
87 such problems, we developed the ReaxFF reactive force field,³
88 which provides nearly the accuracy of the best QM but at a
89 computational cost of solving Newton's equation of motion on
90 nuclei only. This allows us to accurately compute the atomic
91 interactions found in ettringite. Essential elements of ReaxFF
92 include:

- 93 1. an analytic relation between bond order and bond
94 distance and between bond energy and bond order that
95 establishes smooth transitions as bonds form and break
- 96 2. a rule for how charge depends on geometry and atomic
97 character that allows charges to flow continuously as
98 bonds form and break
- 99 3. functional forms that describe well the barrier heights of
100 both allowed and forbidden reactions, including the
101 effects of resonance.

102 ReaxFF partitions the total energy of interactions similarly to
103 those found in nonreactive force fields like Dreiding, that is, in
104 valence, nonbonded, and H-bond terms, but it introduces bond
105 order dependencies on valence terms and additional potential
106 energy corrections to properly describe bond formation and
107 dissociation under different environmental conditions. The
108 overall energy of the system in ReaxFF is given as

$$\begin{aligned}
 U_{\text{Total}} = & E_{\text{bonds}} + E_{\text{angles}} + E_{\text{torsions}} + E_{\text{H-bonds}} \\
 & + E_{\text{vdW}} + E_{\text{Coulomb}} + E_{\text{lp}} + E_{\text{over}} + E_{\text{under}} \\
 & + E_{\text{pen}} + E_{\text{coa}} + E_{\text{C}_2} + E_{\text{triple}} + E_{\text{conj}} \quad (1)
 \end{aligned}$$

109 where E_{lp} corresponds to the lone pair energy penalty based on
110 the number of lone pairs around an atom, E_{over} to the energy
111 penalty for overcoordinated atoms, E_{under} to the energy
112 contribution for the resonance of the π -electron between
113 attached undercoordinated atomic centers, E_{pen} to an energy
114 penalty needed to reproduce the stability of systems with
115 double bonds sharing an atom in a valency angle (e.g., allene),
116 E_{coa} to the three-body conjugation term to describe the stability
117 of $-\text{NO}_2$ groups, E_{C_2} to an energy contribution that captures

the stability of C_2 , E_{triple} to a triple bond stabilization energy in
CO bonded pairs, and E_{conj} to the contribution of conjugation
effects to the molecular energy.

In ReaxFF, each element is described using a single atom
type, even through bonding during a chemical reaction. This
also facilitates the transferability of the parameters. For each
element, several parameters to describe valence bond
parameters, electronegativity, hardness, and other effects are
optimized to reproduce the QM-derived energies and charges.
ReaxFF can reproduce energies near the accuracy of the
training set at a much lower computational cost. The reactive
site or pathways need not be predefined in a ReaxFF MD
simulation, and connectivities between the atoms are not
predetermined. Instead, bond orders are calculated from the
interatomic distances r_{ij} . By using a bond length/bond order
relationship, smooth transitions from nonbonded to single,
double, and triple bonded systems, and vice versa, are obtained.
This requires bond orders to be updated every iteration, for
single (σ), double (π), and triple ($\pi-\pi$) bonds as a function of
interatomic distances (r_{ij}), using scaling parameters $p_{\text{BO},1-6}$
fitted from QM calculations on small representative systems
and making all of the connectivity-dependent interactions
bond-order-dependent to ensure that their energy contribu-
tions disappear upon bond dissociation. Bond orders are
computed initially as

$$\begin{aligned}
 \text{BO}'_{ij} = & \exp \left[p_{\text{BO},1} \left(\frac{r_{ij}}{r_0} \right)^{p_{\text{BO},2}} \right] + \exp \left[p_{\text{BO},3} \left(\frac{r_{ij}}{r_0} \right)^{p_{\text{BO},4}} \right] \\
 & + \exp \left[p_{\text{BO},5} \left(\frac{r_{ij}}{r_0} \right)^{p_{\text{BO},6}} \right] \quad (2)
 \end{aligned}$$

From these (uncorrected) bond orders, BO' , an uncorrected
atomic overcoordination Δ' is calculated as the difference
between the total bond order around the atom and the number
of its bonding electrons, Val , that is

$$\Delta'_i = -\text{Val}_i + \sum_{j=1}^{\text{neighbors}(i)} \text{BO}'_{ij} \quad (3)$$

Equation 3 is then used to obtain corrected bond orders, BO_{ij} ,
and subsequently a new corrected overcoordination. For more
details on the exact functional forms, see the Supporting
Information from ref 4.

The bond energies are then computed from the corrected
bond orders by

$$\begin{aligned}
 E_{\text{bond}} = & -D_e^\sigma \text{BO}_{ij}^\sigma \exp[p_{\text{be}1} (1 - (\text{BO}_{ij}^\sigma)^{p_{\text{be}2}})] - D_e^\pi \text{BO}_{ij}^\pi \\
 & - D_e^{\pi-\pi} \text{BO}_{ij}^{\pi-\pi} \quad (4)
 \end{aligned}$$

where D_e is the corresponding dissociation energy for each
bond type and $p_{\text{be}1,2}$ correspond to atomic parameters that are
fitted from QM calculations on small representative cases.
According to eq 4, the bond energy term E_{bond} gradually
disappears as the bond order BO approaches zero during the
dissociation of a bond. The ij valence angle and torsion angle
energy terms are also functions of bond orders and go to zero
upon bond dissociation. This ensures continuity of the energy
and forces during bond dissociation/formation.

Table 1. Atom Parameters

atom type	EEM parameters			bond order correction				
	χ (eV)	η (eV)	γ (Å)	$P_{ov/un}$	P_{val3}	P_{boc4}	P_{boc3}	P_{boc5}
H	3.7248	9.6093	0.8203	-19.4571	4.2733	3.0408	2.4197	0.0003
O	8.5000	8.3122	1.0898	-3.5500	2.9000	3.5027	0.7640	0.0021
Ca	-1.7130	6.5096	1.0000	-2.0000	3.8301	49.9248	0.3370	0.0000
Al	1.7429	6.8319	0.4265	-22.7101	1.7045	20.0000	0.2500	0.0000
S	5.8284	8.2545	1.0336	-11.0000	2.7466	5.7487	23.2859	12.7147

Table 2. Bond Energy and Bond Order Parameters (D_e in kcal/mol; r in Å)

atom pair	$D_{e,\sigma}$	$D_{e,\pi}$	P_{be1}	P_{be2}	r_σ	P_{bo1}	P_{bo2}	r_π	P_{bo3}	P_{bo4}
Al–O	227.9327	0.0	-0.8375	0.3686	1.5382	-0.1740	5.2057			
S–O	161.0562	220.0	0.6070	0.7150	1.4608	-0.1109	5.4501	1.3987	-0.2741	8.3216

Nonbonded interactions (van der Waals, Coulomb) are calculated between every atom pair, irrespective of connectivity and avoiding excessive close-range contributions by shielding.

ReaxFF parameters have been developed for a variety of materials, including hydrocarbons,³ silicon/silicon oxide,⁵ metals,⁶ metal oxides,⁴ and metal hydrides,⁷ among others. It has also been used to study a variety of complex chemical systems.^{4,8–10}

2.1.1. ReaxFF Force Field for Ettringite. We developed the ettringite ReaxFF force field to accurately reproduce the first-principles QM interactions in hydrous calcium aluminum sulfate systems (H/Ca/Al/S/O) and to provide a way to extend the first-principles accuracy to the much larger length and time scales needed to examine the processes of interest here.

We started with recently derived ReaxFF parameters for Al/O from ref 11 and Ca/O from ref 12. These parameters had been optimized to describe the crystals of various phases of Al and Ca and of various aluminum oxides and calcium oxides. As discussed below, we prepared additional training data to complete the Al, Ca, O, S, and H interactions present in ettringite and validated ReaxFF charges for its constituent molecular motifs against QM Mulliken populations.

This involved performing QM density functional theory (DFT) calculations on representative finite clusters using the B3LYP hybrid functional with the LACVP** basis set using the Jaguar 4.2 package.¹³ The calculation on periodic systems used the PBE functional with double- ζ plus polarization basis of contracted Gaussian functions with SeqQuest.¹⁴ The complete QM-derived force field training set includes EOS, atomic bond energy curves, dissociation energies, angle bend energy curves, and other relevant material properties, such as heats of formation, overcoordination, and others, for all possible interactions between Ca, Al, O, S, H, and H₂O. Angle bend energies in ettringite were also trained to achieve an accurate geometrical representation of the crystal structure. These included Ca–Ca–Ca in a triangle [Ca(OH)₂]₃ bend to represent the potential surface of Ca–O–Ca and O–Ca–O angles, the distance of Al–Al in Ca[AlO₄]₂ scanned to represent the potential surface of the Ca–O–Al angle, which is typical in ettringite along the c direction, the Al–O–S angle in Al(OH)₂–O–SO₃H, and the Ca–O–S angle in CaSO₄ gas.

3. RESULTS AND DISCUSSION

The geometries and energies of the species and complexes in ettringite were calculated using DFT, and the ReaxFF force field parameters were optimized to minimize the differences

between the DFT and ReaxFF energies. Tables 1–5 provide a summary of the ReaxFF force field parameters for ettringite.

Table 3. van der Waals Parameters

atom pair	R_{vdW} (Å)	ϵ (kcal/mol)	α	γ_{vdW}
Al–O	1.8928	0.1745	11.2476	7.3490
S–O	1.7931	0.2047	10.2391	8.2411

The corresponding ReaxFF potential functional forms may be consulted in ref 4. These optimized parameters are available in a ffield file (see the Supporting Information section of ref 4) that can be directly used in the freely available “Large-scale Atomic/Molecular Massively Parallel Simulator” (LAMMPS¹⁵) molecular dynamics program from Sandia National Laboratories.

3.1. Ettringite ReaxFF Force Field Validation. We began by constructing a $2 \times 2 \times 1$ molecular triclinic unit supercell model from the crystal structure determined by Moore,¹⁶ as shown in Figure 1. This molecular model served as the basic structure for the calculations reported here.

Charges play an important role in computing charge distributions and overall electrostatics during bond breaking and formation in ReaxFF. To confirm the accuracy of the net molecular charges calculated with ReaxFF (using the charge equilibration method QEq from Rappe et al¹⁷) on subspecies found in ettringite, including H₂SO₄, CaSO₄, Al(OH)₃, Al(OH)₂–O–SO₃H, and the C₃A₂ cluster, we compared these to Mulliken charge populations. Figure 2 shows that ReaxFF charges for the different species of interest are in close agreement with the QM results.

In addition to validating bond energies, EOS, and other properties, we compared DFT-calculated angle bend energies against equivalent scans using the ettringite ReaxFF force field. Angle bend energies for Ca–O–Ca, O–Ca–O, Ca–O–Al, Al–O–S, and Ca–O–S angles are important to the structural conformity of the model (see Figure 3).

To determine the structural stability and conformity of our model during room-temperature dynamics, the $2 \times 2 \times 1$ ettringite supercell model shown in Figure 1 was equilibrated for 20 ps in an NPT ensemble with RMD calculations at 300 K and a 0.25 fs time step. The last 10 ps were used for statistical calculation of the cell parameters and for computing radial distribution functions (RDFs). The calculated unit cell parameters accurately reproduce the experimental values within ~4%, as shown in Table 6. The total averaged RDFs and all of the RDF pairs were also calculated (Figure 4), revealing

Table 4. Angle Parameters

angle type	$\Theta_{0,0}$ (deg)	P_{val1} (kcal/mol)	P_{val2}	P_{coa1}	P_{val7}	P_{pen1}	P_{val4}
O–Al–O	54.0864	9.7594	1.9476	0.0	3.0000	0.0	1.4400
O–O–Al	34.4326	25.9544	5.1239	0.0	2.7500	0.0	1.7141
H–O–Al	90.0000	19.7491	1.8227	0.0	1.0000	0.0	2.5337
Al–O–Al	23.7270	19.5973	4.0000	0.0	0.6619	0.0	1.9380
Ca–O–Al	79.6174	23.7025	5.7958	0.0	0.9119	0.0	1.6244
Al–O–S	102.1915	7.3381	0.4786	0.0	0.5846	0.0	1.4022
Ca–O–S	114.2370	19.7117	0.5240	0.0	3.0000	0.0	0.8335
O–S–O	81.7931	31.2043	6.5492	−4.4116	2.6067	0.0	3.0000
O–O–S	83.9753	31.0715	3.5590	0.0	0.8161	0.0	1.1776

Table 5. Torsion Angle Parameters (V in kcal/mol)

torsion angle	V_1	V_2	V_3	P_{tor1}	P_{cot1}
H–O–S–O	2.5000	2.5000	0.2237	−10.0000	−1.0000
X–O–S–X	0.1000	50.0000	0.0100	−10.0000	0.0000

247 predicted structures from our MD simulations that are in close
248 agreements with experiments.

249 **3.2. Elastic Constants of Ettringite.** To characterize the
250 stiffness of ettringite, we calculated its elastic constants from the
251 linear relation between the stress and strain tensors in the limit
252 of infinitesimal deformation. We computed the adiabatic
253 constants (at 0 K) considering that the thermal expansion of
254 the unit cell at ambient temperature, relative to that at 0 K, was
255 within the error bars of our method (as estimated from our
256 *NPT*-RMD structure equilibration simulations at 300 K). This
257 involved deforming the unit cell by less than 1% in the different
258 directions of interest and calculating the change in the
259 corresponding stress tensor components. This way, we avoided
260 the higher uncertainty and computational costs of calculating
261 the elastic constants at ambient temperature, which requires
262 time averages of differential properties (e.g., stress tensor
263 components using a canonical or isothermal–isobaric ensemble
264 approach) and balancing the systematic and statistical errors to
265 fully equilibrate the deformed cell before sampling the stress
266 tensor. Table 7 shows that the results from our simulations are

quantitatively consistent with the isothermal elastic constants
reported from experiments.¹⁸

269 **3.3. Atomistic Failure Modes of Ettringite under**
270 **Mechanical Loading.** To understand the failure modes of
271 ettringite, we carried out RMD deformation simulations, with
272 the ReaxFF force field reported here, along the y and z
273 directions on the model system depicted in Figure 1. We
274 started from a relaxed volume $2 \times 2 \times 1$ supercell using *NPT*-
275 RMD at 300 K temperature and 1 atm of pressure. The system
276 was equilibrated at every 1% strain for 20 ps up to 15% strain in
277 the y direction and 20% strain in the z direction, and the last 10
278 ps was used for data collection at each deformation strain.

The uniaxial stress–strain characteristics along the z
279 direction, under compression and tension, are presented in
280 the Figure 5. These results indicate that the true elastic limit
281 along the z direction is at $\sim 3\%$ under strain in compression and
282 $\sim 7\%$ in tension, while failure occurs between 11 and 12%
283 deformation. These results also indicate that in this particular
284 direction, ettringite is more resistant under tensile strain than
285 under compression. We observed hydrogen bonds breaking and
286 re-forming during compression, which accounts for the increase
287 in plastic strain in this mode. The longitudinal elastic
288 anisotropy due to the crystallographic structure is $C_{11}/C_{33} =$
289 0.63, while the shear anisotropy is $C_{66}/C_{44} = 0.6$. The stiff
290 octahedra chains of $[\text{Al}(\text{OH})_6]_3^-$ alternating with triplets of
291 Ca_2^+ in eight-fold coordination along the z -axis lead to higher
292 stiffness in this direction.
293

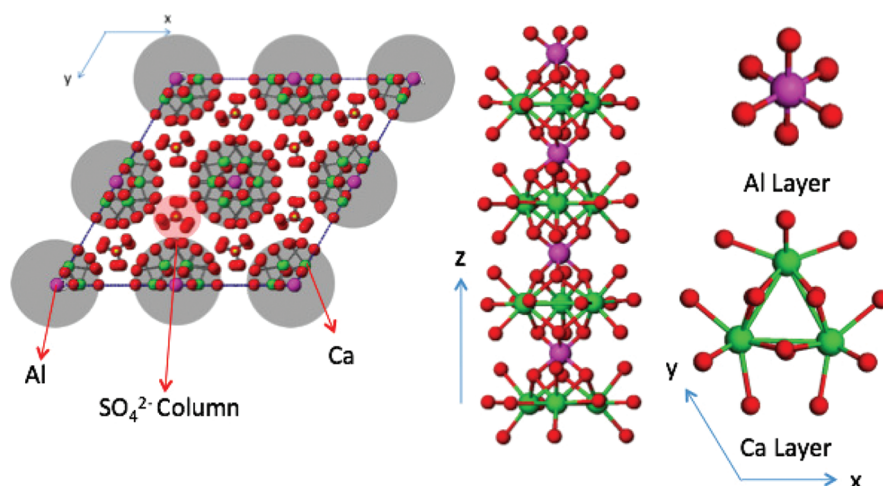


Figure 1. The triclinic $2 \times 2 \times 1$ molecular supercell crystal model of ettringite contains a total of 496 atoms, ignoring hydrogens, arranged in 4 stacked layers (center image) of intercalated Ca and Al sublayers (right image). The left image shows the projection of crystal structure on to the (0001) plane. C3A columns lay parallel to the z -axis (c) with sulfate and water molecules in the intercolumn channels. The SO_4^{2-} groups are located at the interstitials between columns, along with water molecules, and 132 hydrogen atoms (not shown) on the surface of the columns and around the SO_4^{2-} groups neutralize the system.

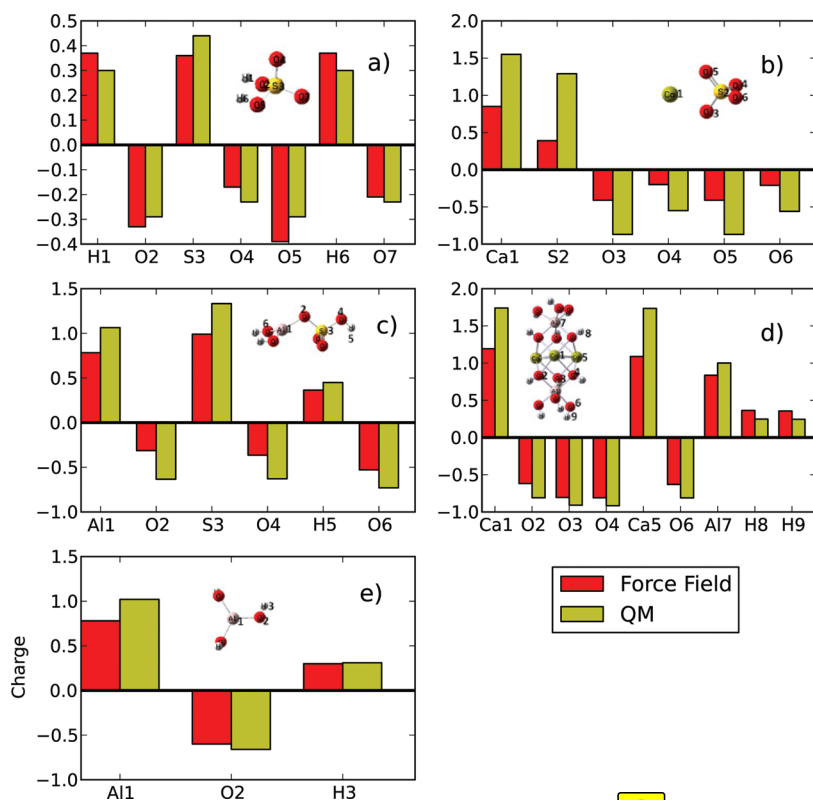


Figure 2. Comparison of the charges for Eettringite from the ReaxFF force field and from QM electron populations for (a) H₂SO₄, (b) CaSO₄, (c) the C₃A₂ cluster, (d) Al(OH)₂-O-SO₄H, and (e) Al(OH)₃.

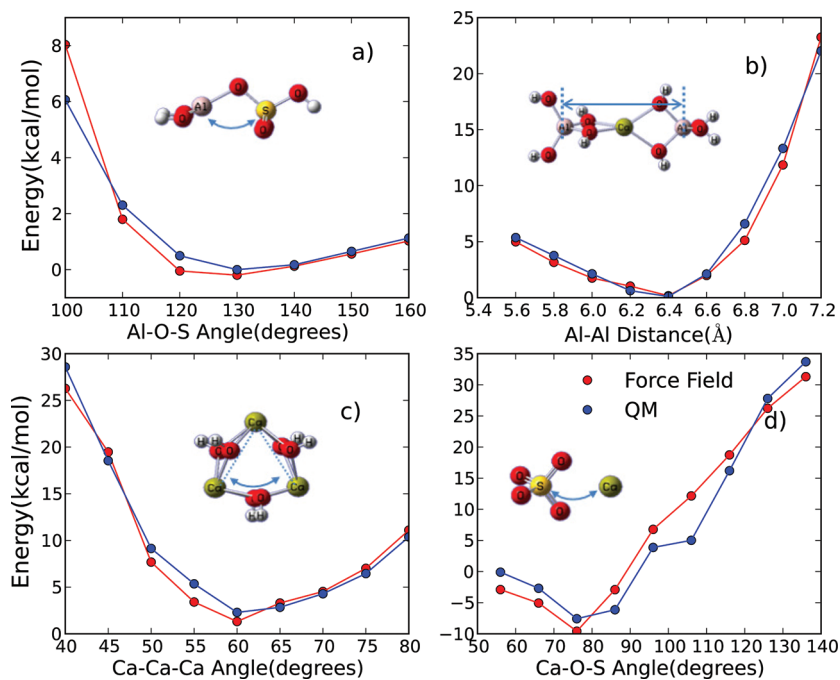


Figure 3. Comparison of the ettringite angle bend energies from ReaxFF and from QM angle scans for (a) Ca-O-Ca and O-Ca-O, (b) Ca-O-Al, (c) Al-O-S, and (d) Ca-O-S angles.

294 The stress-strain characteristics of the system along the *y*
 295 direction are shown in Figure 6. Material failure during
 296 compression in the *y* direction occurs at ~13% strain and at
 297 ~8% strain during tension. The intermolecular hydrogen
 298 bonding network that provides mechanical stability to the

C3A columnar conformation are responsible for the decreased
 299 loading capacity in the *a/b* directions of the material. 300

The number of bond changes during the dynamics of
 301 mechanical strain was used to provide further insight into the
 302 failure mechanisms of ettringite. 303

Table 6. Comparison between Calculated Ettringite Cell Parameters and Experiment

cell parameters	experimental	ReaxFF NPT-RMD
a/b	11.167	11.53
c	21.360	22.22

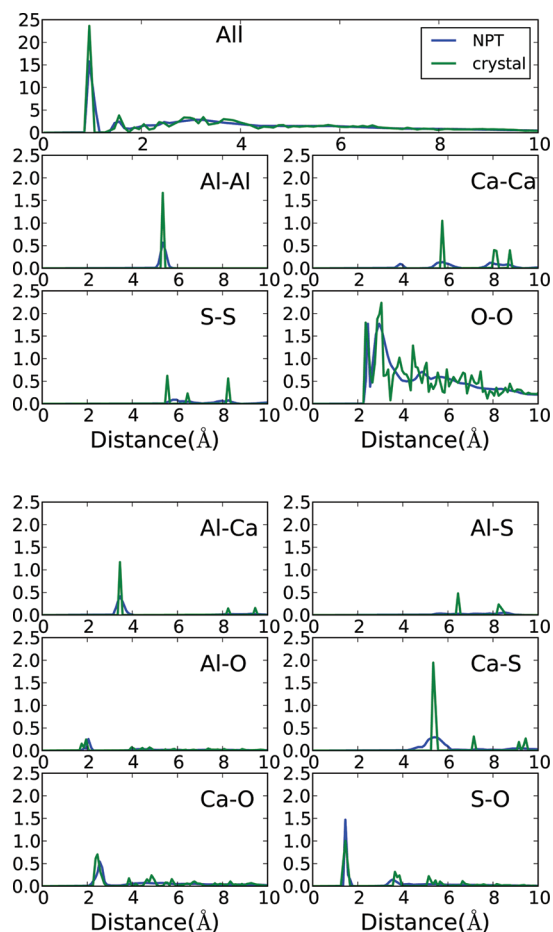


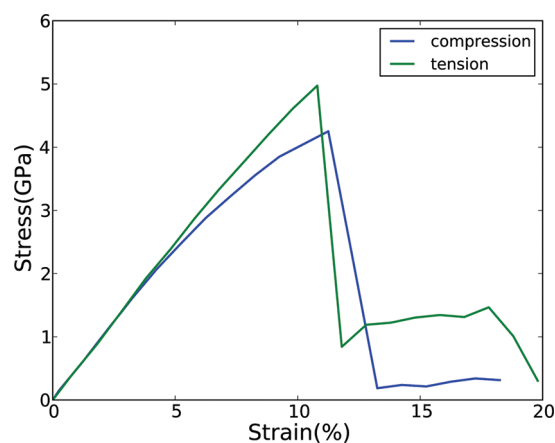
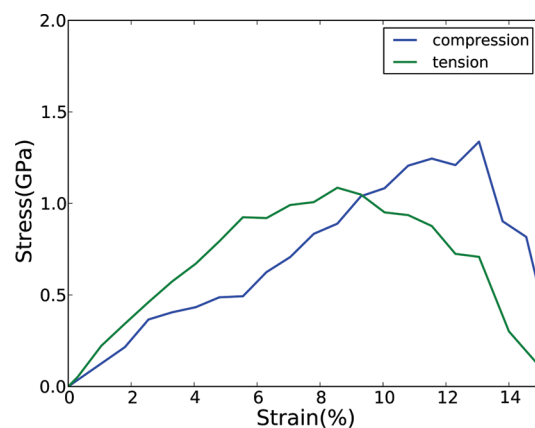
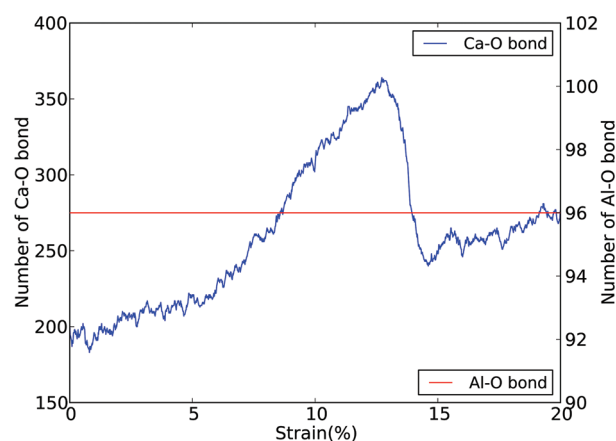
Figure 4. Radial distribution functions (RDFs) for Ettringite; experimental and ReaxFF NPT-RMD simulation results agree.

Figure 7 shows that during the initial stages of compression along the z direction, the number of Ca–O bonds increases slowly until $\sim 7\%$ compression, and they increase at a faster pace thereafter, until the failure point ($\sim 11\%$ strain). On the

Table 7. Computed (Adiabatic) versus Experimental (Isothermal) Elastic Constants in Ettringite Crystal^a

elastic constants	expt ¹⁸	ReaxFF
C_{11}	35.1 ± 0.1	45.4
C_{12}	21.9 ± 0.1	25.0
C_{13}	20.0 ± 0.5	23.0
C_{14}	0.6 ± 0.2	1.9
C_{33}	55 ± 1	53.9
C_{44}	11.0 ± 0.2	11.1
C_{66}	$6.6^* \pm 0.1$	8.1
bulk modulus (K)	27.3 ± 0.9	26.76
shear modulus (G)	9.5 ± 0.8	12.44
Poisson ratio(ν)	0.34 ± 0.02	0.30

^aNote: C_{66}^* is calculated as $(C_{11} - C_{12})/2$.

Figure 5. Stress–strain curve along the z direction under compression and tension deformation.Figure 6. Stress–strain curve along the y triclinic (a/b) direction under compression (blue) and tension (black).Figure 7. The number of Ca–O bonds increases piecewise linearly between 0 and 7% and 7 and 11%, until failure at $\sim 11\%$ elongation in the z direction, while the number of Al–O bonds remains constant during the full range of compression deformation in the same direction.

other hand, the numbers of Al–O bonds do not change during compression; therefore, the failure in this mode is attributed to Ca–O bond breaking in the C3A column. We observe that during tension, the number of Ca–O bonds decreases at a constant rate before reaching the failure point of the material, at $\sim 11\%$ tension, and sharply increases thereafter (Figure 8). The

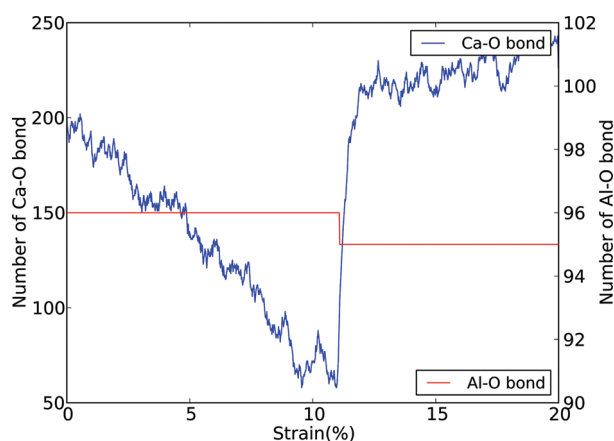


Figure 8. The number of Ca–O bonds decreases linearly during elongation in the z direction until failure at $\sim 11\%$, while the number of Al–O bonds decreases by one at the failure point.

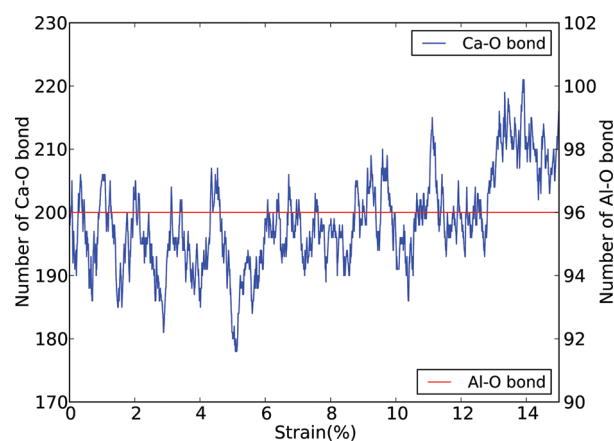


Figure 10. The number of Ca–O bonds changes little during tensile deformation in the y triclinic direction, with a slight increase after failure at $\sim 12\%$.

314 C3A column loses its structural character after one Al–O bond
315 is lost, which occurs after the system's failure point at $\sim 11\%$
316 elongation.

317 From Figures 7 and 8, it is evident that the change in the
318 number of Ca–O bonds is much less than that observed for the
319 z (c) direction. Moreover, these changes are mainly due to the
320 Ca–water interactions because the conformation of the C3A
321 column is not changed during the deformation. The failure
322 mechanism in this case is associated with hydrogen bond
323 breaking between neighboring C3A columns.

324 The monocline structure in ettringite, which causes some
325 shear stress, and hydrogen bond breaking are responsible for
326 the oscillatory nature of Figures 9 and 10.

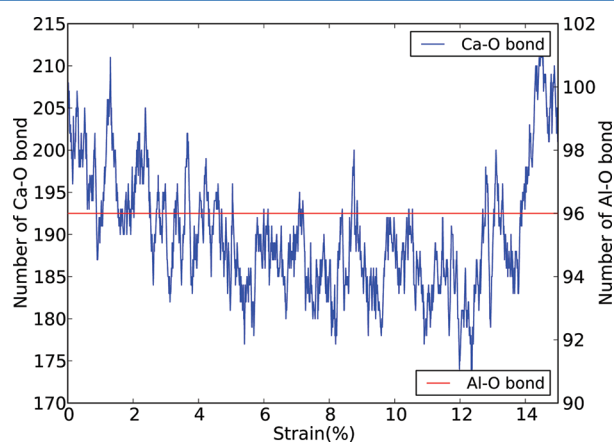


Figure 9. The number of Ca–O bonds decreases linearly during compression in the y triclinic direction, and a small increase is observed after failure at $\sim 12\%$, while the number of Al–O bonds remains constant even after the failure point.

4. SUMMARY AND CONCLUSIONS

327 We have developed and validated a first-principles-derived
328 ReaxFF reactive force field for ettringite and applied it to study
329 the general mechanical properties and atomistic failure
330 mechanisms of the ettringite mineral. In particular, we
331 determined the structural stability and geometry of ettringite
332 at ambient temperature to be in close agreement with

experimental RDFs, its adiabatic elastic constants to be in
333 quantitative agreement with experimentally obtained constants,
334 and from isothermal–isobaric RMD simulations, the sequence
335 of molecular events that lead to its failure under mechanical
336 compression and tension. We found that Ca–O bond breaking
337 in the C3A column leads to failure during compression and
338 tension, while hydrogen bond network formation leads to an
339 increase in plastic strain during compression.

340
341 The results presented here are essential for understanding
342 the role of ettringite in cement and concrete properties. We are
343 now using this ReaxFF force field to study the hydration
344 kinetics of ettringite and the effect of water on ettringite (and
345 delayed ettringite formation, DEF) as it pertains to the long-
346 term degradation of cement paste and concrete properties. This
347 will be the subject of a subsequent publication.

■ ASSOCIATED CONTENT

📄 Supporting Information

Description of the ReaxFF reactive force field developed. This
350 material is available free of charge via the Internet at [http://](http://pubs.acs.org)
351 pubs.acs.org.

■ AUTHOR INFORMATION

Corresponding Author

*E-mail: ajaramil@caltech.edu (A.J.-B.); wag@wag.caltech.edu
355 (W.A.G.).

Notes

The authors declare no competing financial interest.

■ ACKNOWLEDGMENTS

The authors would like to thank Adri van Duin for providing
360 the Al/O ReaxFF parameters and Hegoi Manzano for providing
361 the corresponding Ca/O parameters. L.L. performed the work
362 associated with his contributions in this paper during a visiting
363 appointment at the Materials and Process Simulation Center in
364 Caltech. This material is based on work supported by the
365 Department of Transportation, Federal Highway Administration
366 (FHWA), under Award Number BAA No. DTFH61-09-R-
367 00017. Special thanks to Dr. Kunik Lee from FHWA for HIS
368 support of this program.

370 ■ REFERENCES

- 371 (1) Lee, H.; Cody, R. D.; Cody, A. M.; Spry, P. G. *Environ. Eng.*
372 *Geosci.* **2003**, *9*, 313–326.
- 373 (2) Santhanam, M.; Cohen, M. D.; Olek, J. *Cem. Concr. Res.* **2001**, *31*,
374 845–851.
- 375 (3) van Duin, A. C. T.; Dasgupta, S.; Lorant, F.; Goddard, W. A. J.
376 *Phys. Chem. A* **2001**, *105*, 9396–9409.
- 377 (4) Chenoweth, K.; A.C.T., v. D.; P., P.; Cheng, M.; J., O.; W.A., G. I.
378 *J. Phys. Chem. C* **2008**, *112*, 14645–14654.
- 379 (5) van Duin, A. C. T.; Strachan, A.; Stewman, S.; Zhang, Q. S.; Xu,
380 X.; Goddard, W. A. J. *Phys. Chem. A* **2003**, *107*, 3803–3811.
- 381 (6) Zhang, Q.; Cagin, T.; van Duin, A.; Goddard, W. A.; Qi, Y.;
382 Hector, L. G. *Phys. Rev. B* **2004**, *69*, 11.
- 383 (7) Cheung, S.; Deng, W. Q.; van Duin, A. C. T.; Goddard, W. A. J.
384 *Phys. Chem. A* **2005**, *109*, 851–859.
- 385 (8) Chenoweth, K.; Cheung, S.; van Duin, A. C. T.; Goddard, W. A.;
386 Kober, E. M. *J. Am. Chem. Soc.* **2005**, *127*, 7192–7202.
- 387 (9) van Duin, A. C. T.; Zeiri, Y.; Dubnikova, F.; Kosloff, R.; Goddard,
388 W. A. J. *Am. Chem. Soc.* **2005**, *127*, 11053–11062.
- 389 (10) Nielson, K. D.; van Duin, A. C. T.; Oxgaard, J.; Deng, W. Q.;
390 Goddard, W. A. J. *Phys. Chem. A* **2005**, *109*, 493–499.
- 391 (11) Kim, S.; Persson, P.; Kumar, N.; Sofo, J.; Kubicki, J.; van Duin,
392 A. J. *Phys. Chem. A* **2011**, Submitted.
- 393 (12) Manzano, H.; Buehler, M.; Pellenq, R.; van Duin, A. In
394 preparation for submission.
- 395 (13) *Jaguar*; Schrodinger, LLC: New York, 2011.
- 396 (14) Schultz, P. A.; Muller, P. *SeqQuest Electronic Structure Code*;
397 Sandia National Laboratories: Albuquerque, NM, 2011.
- 398 (15) Plimpton, S. J. *Comput. Phys.* **1995**, *117*, 1–19.
- 399 (16) Moore, A. E.; Taylor, H. F. W. *Acta Crystallogra., Sect. B* **1970**, *B*
400 *26*, 386.
- 401 (17) Rappe, A. K.; Goddard, W. A. J. *Phys. Chem.* **1991**, *95*, 3358–
402 3363.
- 403 (18) Speziale, S.; Jiang, F. M.; Mao, Z.; Monteiro, P. J. M.; Wenk, H.
404 R.; Duffy, T. S.; Schilling, F. R. *Cem. Concr. Res.* **2008**, *38*, 885–889.